

Neural Dynamics Model of Visual Decision-Making: Learning from Human Experts

Jie SU^{1†}, Fang CAI^{1†}, Shu-Kuo ZHAO², Xin-Yi WANG¹,
Tian-Yi QIAN^{1*}, Da-Hui WANG^{2*}, Bo HONG^{1*}

^{1*} Qiyuan Laboratory, Beijing, China.

² School of Systems Science, Beijing Normal University, No. 19,
Xinjiekouwai St., Beijing, 100875, China.

*Corresponding author(s). E-mail(s): qiantianyi@qiyuanlab.com;
wangdh@bnu.edu.cn; hongbo@qiyuanlab.com;

†These authors contributed equally to this work.

Abstract

Uncovering the fundamental neural correlates of biological intelligence, developing mathematical models, and conducting computational simulations are critical for advancing new paradigms in artificial intelligence (AI). In this study, we implemented a comprehensive visual decision-making model that spans from visual input to behavioral output, using a neural dynamics modeling approach. Drawing inspiration from the key components of the dorsal visual pathway in primates, our model not only aligns closely with human behavior but also reflects neural activities in primates, and achieving accuracy comparable to convolutional neural networks (CNNs). Moreover, magnetic resonance imaging (MRI) identified key neuroimaging features such as structural connections and functional connectivity that are associated with performance in perceptual decision-making tasks. A neuroimaging-informed fine-tuning approach was introduced and applied to the model, leading to performance improvements that paralleled the behavioral variations observed among subjects. Compared to classical deep learning models, our model more accurately replicates the behavioral performance of biological intelligence, relying on the structural characteristics of biological neural networks rather than extensive training data, and demonstrating enhanced resilience to perturbation.

Keywords: neural dynamics model, spiking neural network, perceptual decision-making, magnetic resonance imaging, neuroimaging-informed fine-tuning

1 Introduction

Abstracting the structures of biological neural systems into mathematical models and constructing artificial neural networks based on these abstractions to address real-world problems, represents a pivotal approach to innovation in artificial intelligence. Over the past decades, this approach has achieved significant success in various fields such as pattern recognition and computer vision [1–5]. Visual perception, a fundamental process through which humans and animals interpret and interact with the environment, is a central topic in both neuroscience and artificial intelligence (AI). Understanding the neural mechanisms underlying perceptual decision-making not only provides insights into biological systems but also has the potential to drive advancements in AI technologies. Convolutional neural network (CNN) models, inspired by the receptive fields and parallel distributed processing in animal vision systems, have achieved notable success in tasks such as object detection, facial recognition [6–8], and action recognition [9, 10], often surpassing human performance. However, these models face significant limitations, including the need for vast amounts of labeled data, lack of biological interpretability, and susceptibility to adversarial attacks. These limitations highlight the gap between current AI systems and biological neural networks regarding robustness, efficiency, and flexibility. Addressing these challenges requires a paradigm shift towards models that more closely mimic the underlying principles of biological neural computation.

Motion perception is critical for animals to detect potential conspecifics, preys or predators, and is vital for their survival. The motion perception system starts with retinal input, travels through the lateral geniculate nucleus (LGN) to the primary visual cortex (V1), and then projects to parietal areas along the dorsal visual pathway, supporting spatial attention and eye movements [11]. Direction-selective (DS) neurons are widely present in brain areas such as V1, middle temporal area (MT), and lateral

intraparietal area (LIP) [12–14], which are essential for motion perception. The direction preference of V1 DS neurons depends on the spatial pattern of LGN neurons to which they are connected [15, 16]. Motion perception relies on the integration of both spatial and temporal dimensions of information [17]. Spatial integration is achieved by the larger receptive fields of MT neurons [18, 19], while temporal integration primarily relies on the temporal integration properties of LIP neurons [12, 20].

Based on the physiological structures and properties of neurons and circuits in the LIP area, Wang proposed a recurrent neural circuit model [21]. Within this model, two groups of direction-selective excitatory neurons are capable of integrating lower-level synaptic inputs and performing cognitive tasks through recurrent excitation and mutual inhibition mechanisms. The model’s attractor dynamics enhance its ability to perform decision-making and working memory tasks, replicate neural activity patterns observed in non-human primates, and achieve performance consistent with experimental data. Subsequent researches have extended the model by focusing on its simplification, theoretical analyses and training methodologies [22–25]. These studies primarily emphasize fitting and interpreting biological experimental data, showcasing significant biological plausibility and interpretability. However, neuron parameters are usually determined based on averaged experimental data, without considering the physiological characteristics that underlie behavioral differences among individuals. Moreover, the model has not been optimized based on biological features found in primates, which limits its impact and application in artificial intelligence.

Numerous studies have investigated the relationship between the physiological or structural features of the human brain and behavior [26]. These studies span various human behaviors, including cognitive functions such as working memory [27], language acquisition [28], theory of mind [29], and social functions like social network size [30]. Some research examines differences in physiological characteristics between healthy and diseased groups, for example, correlations between neurodegenerative diseases and

physiological indicators of white matter fiber tracts [31–33]. Modern neuroimaging technologies provide effective tools for quantifying human brain physiological features, including gray matter volume [34], cortical thickness [35], and myelination [36] calculated from structural images, measurements of white matter areas from diffusion images [37], and the correlation of blood-oxygen-level-dependent (BOLD) signals between brain areas in resting state, known as resting-state functional connectivity (rest FC) [38–40]. These studies have revealed correlations between brain structure, functional characteristics, and human behavior, contributing to understanding disease mechanisms [41]. Despite these insights, neuroimaging data has not been fully integrated into the development or optimization of artificial neural network (ANN) models. Integrating neuroimaging data with ANN models offers a promising frontier for creating brain-inspired AI models that replicates the behavioral performance of human subjects.

Addressing the gap in biologically inspired dynamics modeling in artificial intelligence applications, specifically the lack of tuning mechanisms integrated with behavioral and neuroimaging data, this study synthesizes known neural mechanisms to construct a comprehensive biological neural dynamics model of visual motion perception. The model adheres to the physiological features of non-human primates and facilitates cognitive decision-making behavior in the Random Dot Kinematogram (RDK) task, exhibiting biological-like behavioral and neuronal characteristics. Furthermore, this study explores the correlation between behavioral and neuroimaging features of human subjects during visual decision tasks through magnetic resonance imaging (MRI) techniques, particularly focusing on the structural and functional characteristics of corresponding brain regions in human experts. Finally, we introduce a novel *neuroimaging-informed fine-tuning* approach, which leverages these neuroimaging characteristics to optimize the artificial biological neural network model and achieve notable improvements in performance.

2 Results

2.1 A Neural Dynamics Model of Visual Decision-Making with Behavioral Performance and Neural Activities Similar to Primates

We constructed a neural dynamics model that encompasses the four key brain areas of the dorsal visual pathway (LGN, V1, MT, and LIP, Figs. 1a-c). This model forms an artificial biological neural network capable of motion perception and performing the Random Dot Kinematogram (RDK) task. The neurons in our model adopt the Leaky Integrate-and-Fire (LIF) model and are interconnected through excitatory synapses (AMPA, NMDA) and inhibitory synapses (GABA) (see § 4.2). The spikes of different neuron groups were recorded during the RDK task (Fig. 1d-f).

The electrophysiologic recordings show that V1 neurons exhibit direction selectivity, which is further enhanced in the MT neurons. In the LIP area, neurons that prefer a specific motion direction gradually dominate, while those favoring the opposite direction are suppressed, resulting in a “*winner-take-all*” effect. Additionally, V1 and MT neuron activation increases with motion coherence but stabilizes during the stimulus period. In contrast, LIP neurons show a gradual ramping of activation, with the ramping speed proportional to motion coherence (Fig. 1d-f). These simulated neural activities closely resemble those recorded in electrophysiological experiments with macaque monkeys [13, 42], demonstrating the biological plausibility of our model.

The performance of our model was evaluated using the entire Random Dot Kinematogram (RDK) dataset (see § 4.1). We calculated the choice probability and average reaction time for each coherence level. Fig. 2a (upper panel) presents the psychometric curve of the model (in blue), which is similar to the psychometric curves of human subjects (in orange). The model’s sensitivity (slope of the psychometric curve, k in Equation 1) is 19.31 ± 0.17 (mean \pm SEM of 45 experiments), significantly exceeding

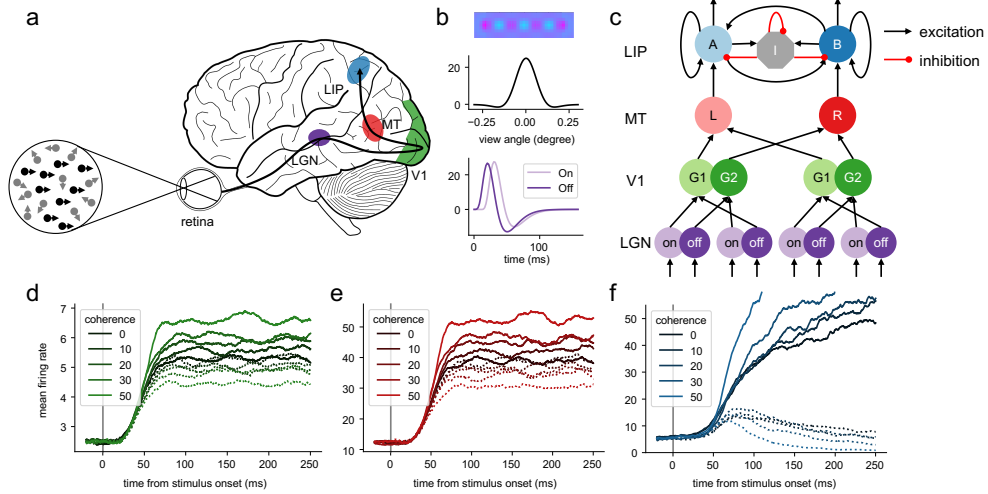


Fig. 1 A neural dynamics model of motion perception inspired by the dorsal visual pathway. **a.** The Random Dot Kinematogram (RDK) and the locations of the key structures within the dorsal visual pathway associated with motion perception and decision-making in the human brain. **b.** Spatial characteristics and arrangements of LGN *ON* and *OFF* neurons, including their spatial and temporal profiles. **c.** Structure of the biologically inspired neural dynamics model, illustrating four modules corresponding to those key brain regions and the connections between them. **d-f.** Averaged firing rates of distinct groups of neurons in response to the RDK stimulus. Time 0 marks the stimulus onset. The solid line represents neuron groups with a preferred directional bias, while the dotted line represents neuron groups with an opposite bias. Color and legend indicate coherence levels. **d.** V1 neurons demonstrate direction selectivity; **e.** MT neurons enhance this selectivity, with the activation of direction-preference neurons increasing with coherence; **f.** LIP neurons exhibit the ramping activity and a *winner-take-all* effect, with the slope of ramping increasing as coherence levels rise.

the average level of human subjects (36 subjects, 15.1 ± 1.9 , $t = 2.50$, $p = 0.015$, two-sample t -test). Moreover, the model's decision time curve aligns with the reaction times of human subjects. As coherence increases (task difficulty decreases), the decision time gradually becomes shorter, as illustrated in Fig. 2a (lower panel).

In electrophysiological experiments, microstimulation of specific brain regions can induce behavioral changes [13, 42]. To verify whether our neural dynamics model exhibits similar characteristics to biological motion perception systems, we conducted virtual cortical stimulation experiments. External currents were injected into different groups of neurons in our model to investigate if the results matched those observed in biological experiments [13, 42].

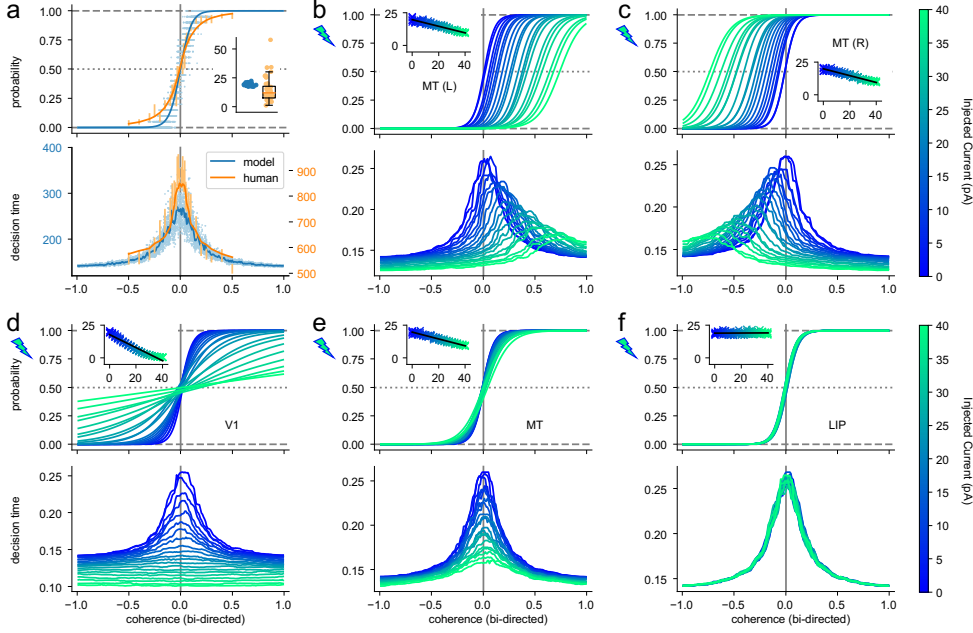


Fig. 2 Behavioral performance of the model in RDK tasks and effect of virtual electrical stimulation. **a.** Behavioral performance of the model and human subjects in the RDK task, showing selection probability, and average reaction time as functions of coherence level (upper: psychometric curve, lower: decision time curve). The model’s performance is represented in blue (average of 45 repetitions), and human performance is shown in orange (average of 36 subjects). Error bars denote the standard error of the mean (SEM) across all subjects. The inset subplot displays the distribution of sensitivity (k) for all subjects (orange) and the model (blue, repeated 45 times). **b.** When additional current (0 pA to 40 pA) is injected into the ‘L’ group of neurons in the MT area of the model, the psychometric and decision time curves shift rightward, sensitivity decreases (slope= -0.25 , $p < 0.001$), and reaction time shorten. Color and colorbar represent the intensity of stimulation, consistent throughout. **c.** Injecting additional current into the ‘R’ group of neurons in MT results in a leftward shift in the psychometric and decision time curves, with decreased sensitivity and decision time (slope= -0.26 , $p < 0.001$). **d.** Performance changes when additional electrical stimulation is applied to all neurons in the model’s V1. The additional input current decreases the slope of the psychometric curve (indicating reduced sensitivity, slope= -0.50 , $p < 0.001$) and reduces mean decision time. **e.** Sensitivity and decision time both decrease when additional electrical stimulation is applied to all neurons in MT (slope= -0.26 , $p < 0.001$). **f.** Applying the same intensity of current to LIP has negligible effects on the model’s performance (slope= 0.005 , $p = 0.60$).

Applying continuous extra current (0 pA to 40 pA, Fig. 2b) to MT neurons that prefer leftward motion shifted the model’s psychometric curve to the right, indicating an increased leftward choice preference (slope= -0.18 , $p < 0.001$). This manipulation slightly reduced the model’s sensitivity (slope= -0.25 , $p < 0.001$), and altered decision times, decreasing for leftward and increasing for rightward motions, aligning with observations in animal studies [42]. Conversely, applying extra current to neurons that

prefer rightward motion resulted in a leftward shift of the psychometric curve and a corresponding leftward shift in the decision time curve (Fig. 2c, intercept changed with external currents: slope=0.18, $p < 0.001$; sensitivity changes with external currents: slope=-0.26, $p < 0.001$). Moreover, when stimulating both groups of neurons in the MT region without selection (0 pA to 40 pA), the model’s sensitivity slightly declined (slope=-0.26, $p < 0.001$), but the decision time notably reduced (Fig. 2e). Correspondingly, stimulating all neurons in the V1 region significantly altered the model’s sensitivity (slope=-0.50, $p < 0.001$) and decision time (Fig. 2d). However, stimulating all excitatory neurons in the LIP area did not affect the model’s sensitivity (slope=0.005, $p = 0.60$) or decision time (Fig. 2f).

2.2 Model Optimization Inspired by Structural Connectivity of Human Experts

Structural connectivity estimated from neuroimaging techniques reflects the mesoscopic properties of fibers, which are directly related to behavioral outcomes [26–30]. To identify the key parameters influencing the task performance, we collected behavioral and neuroimaging data from 36 human subjects performing the RDK tasks.

In the correlation analysis, we found a significant negative correlation between the mean fractional anisotropy (FA) value of white matter in the left lateral occipital region and subjects’ behavioral performance ($r = -0.435$, $p = 0.008$, uncorrected Pearson correlation, Fig. 3a). This indicates that subjects with lower mean FA values in this area performed better in the behavioral experiment. The lateral occipital region, located in the occipital lobe, includes white matter pathways connecting the primary visual cortex and the MT area. Lower FA values may reflect reduced anisotropy and predict a denser distribution of fiber bundles in this region.

The relative white matter volume in the right inferior parietal region (i.e., the ratio of ROI volume to total brain volume, estimated from MR T1 images) was also

significantly positively correlated with subjects' behavioral performance ($r = 0.373$, $p = 0.025$, uncorrected Pearson correlation, Fig. 3c). This suggests that subjects with better performance had a larger white matter volume in this area, indicating a broader range of fiber tracts. The inferior parietal region, located between the occipital and parietal lobes, includes the white matter pathway connecting the MT and LIP regions, which might be associated with decision-making in the brain. These results demonstrate correlations between behavioral performance and the structural features of the visual dorsal pathway. No other structural features showed significant correlations.

In response to key parameters identified in MRI studies, specifically the white matter connections from V1 to MT and from MT to LIP, which influence behavioral performance, we employed a *neuroimaging-informed fine-tuning* approach to adjust model parameters based on MRI analysis results. For the mean FA of left lateral occipital area (Fig. 3a), we modified the average connection weight of the V1-to-MT connections in the model (Fig. 3b, upper panel) accordingly. Increasing the connection weight at lower strengths (mean of the connection matrix gradually increasing to 2) enhanced model sensitivity and reduced decision times, aligning with the observed behavioral correlations. However, further increases in the connection weight led to reduced decision times but a decline in sensitivity (Fig. 3b, lower panel). Similarly, adjusting the connection ratio between MT and LIP neurons (Fig. 3d upper panel) revealed that increasing the ratio from low levels improved model sensitivity and reduced decision times, aligning with neuroimaging and behavioral correlations. However, beyond a certain range, further increases in the connection ratio decreased both model sensitivity and decision times (Fig. 3d lower panel).

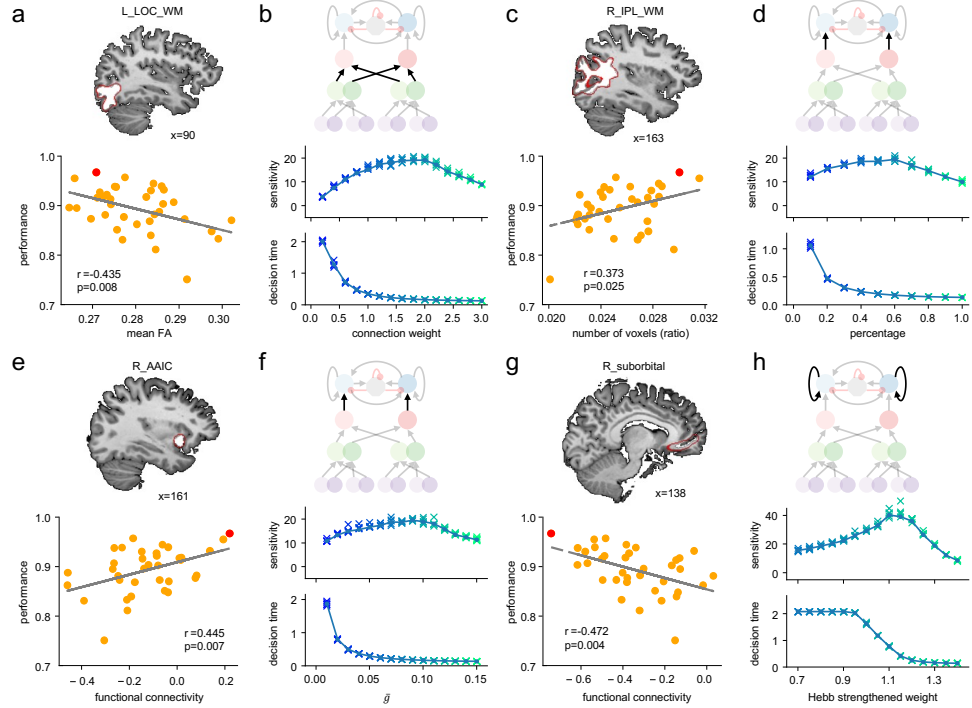


Fig. 3 *Neuroimaging-informed model tuning.* **a.** Mean FA values of the left lateral occipital area in V1 were negatively correlated with subjects' task performance. The red dot represents the best-performing subject (hereinafter the same). Subjects who exhibited lower anisotropy (higher fiber bundle density) in this region performed better in the task. **b.** Tuning the average connection weight between V1 and MT in the model improved accuracy and efficiency within a specific range. Upper: Schematic diagram of the adjusted V1–MT connection. Lower: Increasing the connection weight initially improves model sensitivity and reduces decision time, but later stages show a decrease in sensitivity while decision time continues to decrease. **c.** The white matter volume in the right inferior parietal lobe, located between the occipital and parietal lobes, was positively correlated with task performance. This indicates that subjects with better performance had larger white matter volume relative to total brain volume. **d.** Tuning the proportion of connections between MT and LIP within a specific range improved the model's accuracy and efficiency. Upper: Schematic diagram of the adjusted MT–LIP connection. Lower: Increasing the connection ratio initially enhances sensitivity and reduces decision time, but excessive connections can decrease sensitivity. **e.** Resting-state functional connectivity between MT and AAIC in the right hemisphere was positively correlated with task performance. The positive connectivity may reflect enhanced self-monitoring during the task, leading to improved performance. **f.** Increasing the average synaptic conductivity in MT within a specific range improved the model's sensitivity and efficiency. Upper: Schematic diagram of the adjusted MT–LIP connections. Lower: As conductivity increases, sensitivity initially rises and decision time decreases, but sensitivity eventually declines despite continued reduction in decision time. **g.** Functional connectivity between LIP and the suborbital region in the left hemisphere was negatively correlated with task performance. The negative connectivity may reflect increased engagement during the task, which could lead to improved performance. **h.** Increasing the *Hebb-strengthened weight* between LIP excitatory neurons within a specific range improved the model's sensitivity and efficiency. Upper: Schematic diagram of the adjusted LIP recurrent connections. Lower: Increasing the weight initially enhances sensitivity and reduces decision time, but excessive weight can decrease sensitivity. The Pearson correlation (uncorrected) was used for these analyses; *p*-values are reported.

2.3 Model Optimization Inspired by Functional Connectivity of Human Experts

The correlation between the functional connectivity indicators and the behavioral performance in human subjects was also analyzed. We found a significant positive correlation between behavioral performance and resting-state functional connectivity (FC) of the MT region and the anterior agranular insular complex (AAIC. $r = 0.445$, $p = 0.007$, uncorrected Pearson correlation, Fig. 3e). The resting-state FC between the two brain regions was more positively correlated in subjects with better performance, which could indicate enhanced self-monitoring during the task.

The resting-state FC between the LIP region and the suborbital region of the prefrontal lobe was significantly negatively correlated with behavioral performance ($r = -0.472$, $p = 0.004$, uncorrected Pearson correlation, Fig. 3g). This suggests that a stronger negative correlation between resting-state activities in these regions is associated with better performance, possibly reflecting higher engagement or attentiveness during the task. No significant correlations were observed between the resting-state FC features of other regions and subject behavior.

The functional MRI results highlighted brain areas not included in the existing dynamics model. These regions may provide top-down control to areas involved in motion perception and decision-making, thereby affecting perceptual decisions and behavior. Based on findings from electrophysiological experiments [43], we simulated the modulation of the MT region by adjusting synaptic conductance in this module, without adding new brain regions to the model. The results are illustrated in Figs. 3f and h. Increasing MT synaptic conductance enhanced model sensitivity and reduced decision time, aligning with observed subject behavior. However, beyond a certain point, further increases in connection strength led to decreased sensitivity despite reduced decision time. Similarly, we simulated the regulation of the LIP region by adjusting connection efficiency between DS neurons. This simulation, detailed in

Fig.3h, showed that increasing connection efficiency improved model performance and reduced decision time, but excessive efficiency negatively affected performance.

These experiments illustrate how adjusting model parameters based on structural and functional features can enhance the neural dynamics model, reflecting biological behaviors observed in neuroimaging studies. This approach not only validates the model’s biological plausibility but also introduces a novel method for incorporating neuroimaging data into the fine-tuning of artificial neural networks, which we term *neuroimaging-informed fine-tuning*.

2.4 Superior Robustness of Neural Dynamics Model Under Perturbation

To assess the robustness of our model, we conducted four types of perturbation experiments on both the neural dynamics model and the convolutional neural network model, as described in Section 4.7. Noise was introduced by either discarding or adding noise to the connection weights or neurons in each module of the models. Figs. 4b–i show the changes in accuracy of the CNN and neural dynamics models at each layer with varying perturbation intensities (see Table 1 for statistics, and Extended Fig. 2 for changes in sensitivity).

From these figures, it is evident that our neural dynamics model performs better compared to the CNN model under perturbation. The CNN’s accuracy typically declines more significantly with increased perturbation, whereas the neural dynamics model remains more stable overall. Notably, the model’s performance remains largely unaffected when noise is introduced into modules corresponding to higher-level brain regions. For example, discarding connections from MT to LIP (Fig. 4f, red) or adding noise to these connections (Fig. 4g, red) has minimal impact on model accuracy, far less than the perturbation effects on the CNN (Figs. 4b&c, red). Adding noise to the

input current of neurons almost does not affect the neural dynamics model’s performance (Fig. 4i, except the purple). Adding noise to LGN neurons causes model failure (Figs. 4g&i, purple), likely due to the sparse connections between V1 and LGN leading to over-reliance on LGN signals. Discarding neurons in the decision layer LIP (Fig. 4g, blue) also drastically reduces model performance, as too few LIP neurons cannot maintain the attractor states corresponding to decisions, causing the model to rapidly degrade to a resting state with a single attractor [44], effectively rendering it unable to make decisions.

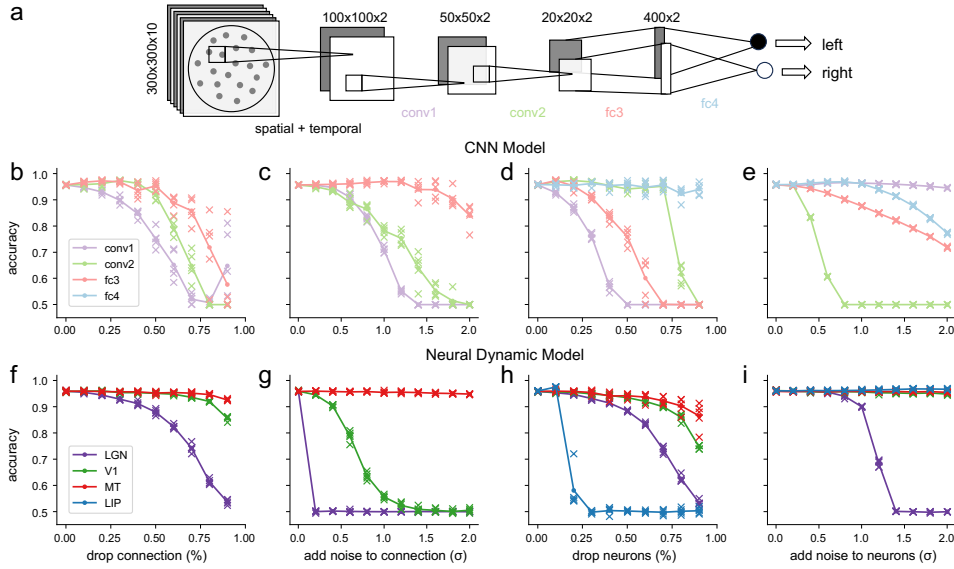


Fig. 4 Comparison between *CNN* and the neural dynamics model in terms of perturbation. **a.** The structure and parameters of the *CNN* model. **b-e.** In the *CNN* model, changes in accuracy under different perturbation conditions: **b.** when a certain percentage of connections are dropped in each layer; **c.** when zero-mean Gaussian noise (with variance as a multiplier of the average absolute value) is added to the connection weights; **d.** when a certain percentage of neurons are dropped; and **e.** when zero-mean Gaussian noise is added to the neuron activations. The colors represent the various parameter layers of the network (b, c, excluding the fully connected layer) or the presynaptic neurons (d, e). Cross marks indicate the accuracy of individual experiments, while the curves represent the overall accuracy averaged across five experiments. **f-i.** In the neural dynamics model, changes in accuracy under similar perturbation conditions: **f.** when a certain percentage of connections are dropped in each layer; **g.** when zero-mean Gaussian noise is added to the connection weights; **h.** when a certain percentage of neurons are dropped; and **i.** when zero-mean Gaussian noise is added to the neuron activations. The colors represent the neurons in each layer (h, i) or the connections emanating from each layer (f, g).

Additionally, we found that changes in accuracy and sensitivity with added noise in the neural dynamics model are consistent, which contrasts with the behavior observed in CNN. In some cases, the CNN model retains high sensitivity, but its accuracy significantly decreases with increasing model bias. Furthermore, the CNN model exhibits greater variation with perturbation (see scatter distribution in Figs. 4b–d, see also Extended Figs. 3, 4), while the neural dynamics model shows smaller bias and maintains relatively stable performance even when disturbed. Unexpectedly, reducing the number of LIP neurons (Extended Fig. 2g, blue) and adding noise to LIP neuron input currents (Extended Fig. 2h, blue) may improve model performance. This is because our base model is not fully optimized; weakening LIP neuron recurrent connections or increasing Ornstein–Uhlenbeck noise may improve performance, thus similar changes in perturbation may also enhance model performance.

3 Discussion

In this study, we developed a neural dynamics model for motion perception and decision-making that simulates the visual dorsal pathway. The model incorporates biomimetic neurons and synapses with dynamic characteristics and kinetic properties as its core elements. These components enable the model to exhibit neural activities and behavioral outputs that are comparable to those of the biological brain, including responses to virtual electrical stimulation. By leveraging neuroimaging insights such as the structural features identified from human experts, we employed neuroimaging-informed fine-tuning to optimize the model parameters, leading to improved performance. Compared to CNNs, our model achieves similar performance with fewer parameters, more closely aligns with biological data, and exhibits greater robustness to perturbations.

Parameter optimization for neural dynamics model is both critical and challenging due to the complexity of nonlinear dynamic systems. Previous studies have primarily

employed data fitting techniques using neural or behavioral data, which are feasible for small-scale models. However, as neural dynamics models increase in scale and complexity, with larger number of parameters and higher computational demands, optimization become significantly more computationally intensive and difficult. While it is theoretically possible to optimize key parameters in some simplified models through analytical methods, such method is generally impractical for more complex models. This study, for the first time, explores the application of neuroimaging data in model optimization, a process we term *neuroimaging-informed fine-tuning*. While this approach may not achieve the global optimum, it offers practical directions for parameter optimization and significantly reduces the search space. It is noteworthy that excessive adjustments to parameters can impair model performance. This observation implies the existence of an optimal range for these parameters that maximizes performance. Biological neural systems, refined over billions of years of evolution, regulate these parameters within such an optimal range, with minor variations accounting for individual differences.

Targeting neuroimaging-informed fine-tuning, we identified brain regions associated with visual decision-making in human subjects through behavioral and imaging experiments. Subjects exhibiting superior performance in visual tasks tend to have lower mean FA values in the occipital region, indicating a higher degree of neural branching in the lateral occipital area. Variations in white matter characteristics within the adults are thought to result from inherent brain structure and the long-term maturation process from childhood to adulthood [45], suggesting that individuals with advanced visual capabilities likely have undergone extensive training and development in visual function. We also identified correlations between the functional connectivity of MT-AAIC and LIP-suborbital with behavioral performance. Variations in functional connectivity between subjects are primarily influenced by their level of participation and cognitive engagement during experiments [46], suggesting that

expert subjects are more engaged and attentive during tasks. We hypothesize that this process involves top-down regulation from higher-level brain areas to task-related regions, potentially enhancing synaptic transmission efficiency. The structural and functional connectivity features observed in human subjects account for their superior performance from the perspectives of innate structure, long-term development, and short-term participation. These findings, applied to key parameter adjustments in the model, indicate that the neural dynamics model aligns with biological intelligence and shows good interpretability in physiological terms. This proposes a potential path for enhancing the model’s performance through neuroimaging-informed fine-tuning.

In the model, LIP Neurons primarily rely on differences in input currents for decision-making. Larger input currents enable the model to reach the decision threshold more quickly but reduce accuracy. For instance, increasing the connection strength between V1 and MT, between MT and LIP, or increasing the number of MT neurons connected to LIP enhances the total currents received by LIP neurons (see Fig 5a). This enhancement improves signal differentiation among neuronal groups that prefer different directions, thereby increasing accuracy (see Fig 3b&d, first half). However, larger input currents cause attractors in decision space to shift towards the diagonal (see Fig. 5b, from 2 to 3) [44]. In this scenario, inhibitory neurons are less effective at suppressing DS neurons that prefer the opposite direction, disrupting the *winner-take-all* dynamics and deteriorating model performance (see Figs. 3b&d, second half).

Similarly, modifying the recurrent connection weights among LIP neuronal groups alters the energy landscape of the decision space. Stronger recurrent connections eliminate the resting states attractor and expand the size of the decision state attractors (see Fig. 5c) [44]. This modification improves performance during the initial phase (see Fig. 3h, first half), but excessively large decision attractors can lead to rapid decision-making in the presence of noise, thereby reducing accuracy (see Fig. 3h, second half).

Adjusting the number of LIP neurons also alters the energy characteristics in the decision space. If the parameters result in stable decision-state attractors, the model can make decisions and maintain the states without external stimuli, demonstrating a degree of working memory capability. This enables decision-making with limited information by integrating noisy evidence, which can shorten decision time but introduces a risk of errors. Conversely, if only one resting state attractor exists, the model fails to reach the decision threshold under any stimulus and cannot make decisions, as evidenced by the perturbation experiment (Fig. 4h, blue), where we deliberately chose the preferred direction associated with higher firing rate neurons for decision. In real-world scenarios, the model would not make a choice in this situation. Similarly, parameter adjustments can lead to another monostable mode, where neuron groups preferring opposite directions both exhibit high firing rates, resulting in an inability to make reasonable decisions (Figs. 4g&i, purple).

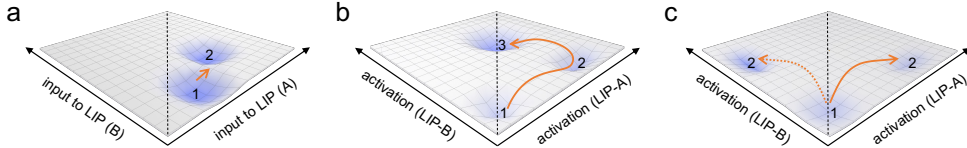


Fig. 5 Diagram showing the impact of parameter adjustments on the model. **a.** Adjusting connection weights shifts the input currents received by the two groups of direction-selective neurons in LIP from state 1 to state 2, thereby increasing both the differences in input currents between the two groups and their absolute magnitudes. **b.** Changes in the information received by LIP affect the energy landscape and attractors in the decision space. Insufficient input currents fail to trigger a decision, maintaining LIP neurons at state 1; optimal input currents and current differences drive the state transition to decision state 2; excessively large input currents cause the state to shift towards 3, deviating from the intended decision state. **c.** Changes in LIP’s recurrent connections also alter the landscape and attractor states in the decision space. Insufficient recurrent connections result in weak evidence being unable to drive LIP from resting state 1 to decision state 2; excessive recurrent connections cause the resting attractor state 1 to disappear and enlarge the attraction basins of decision states 2 and 3, where weak inputs or noise can drive LIP to one of these decision states.

In 2-alternative forced choice (2-AFC) tasks, researchers often model decision-making as evidence accumulation over time, using approaches such as the drift diffusion model (DDM) [47–49], racing diffusion model [50, 51], and linear ballistic

accumulator (LBA) model [52]. The temporal integration in the LIP module resembles the DDM (see discussions in [21–23, 53]), and can be directly related to it [54, 55]. This type of evidence accumulation is not present in feedforward DCNN models. Additionally, the dynamic nature of the LIP constitutes an attractor network [22], where, through iterative processes, the network’s state stabilizes near attractors. This differs fundamentally from traditional DCNNs, which categorize through spatial partitioning within representational spaces, and may explain why neural dynamics models exhibit better stability and noise resistance.

In summary, integrating neural dynamics into AI models can bridge the gap between biological intelligence and artificial systems, leading to the development of next-generation AI that is both interpretable and resilient like biological organisms. By leveraging advances in neuroscience to construct models with neural dynamics, we are able to create AI systems that better mimic biological behavior. The neuroimaging-informed fine-tuning method enhances performance while preserving the advantages of neural dynamics. This approach ensures both high performance and explainability, aligning with biological plausibility and computational efficiency. This synthesis between advanced AI techniques and in-depth neuroscientific insights represents a promising direction for future research and development in both fields.

4 Methods

4.1 The RDK Dataset

Random Dot Kinematogram (RDK) is a classic and common psychophysical paradigm used to study visual motion perception. In a typical RDK stimulus, numerous small dots are randomly distributed on the screen moving at different speeds in different directions, without a clear pattern. This randomness is crucial, preventing subjects from relying solely on local motion cues to judge overall motion characteristics. Typically, a certain proportion of dots (signal dots) move in a specified direction (target

direction), while the remaining dots (noise dots) move randomly [56, 57]. Movement in a fixed direction is referred to as coherent motion, and observers’ ability to report the direction of coherent motion increases with the percentage of coherent motion dots, accompanied by shorter reaction times. This proportion known as coherence, is a measure of task difficulty [58], making it the most important control parameter in RDK stimuli. RDK can conveniently control the relative saliency of motion stimuli, making it suitable for coherence threshold detection or measuring changes in subject behavior with coherence.

In a 2-alternative forced choice (2-AFC) task, with the proportion of coherent motion or its logarithm as the independent variable, a psychometric curve can be plotted showing the probability of a subject choosing a certain direction. This curve typically follows a sigmoid shape and can be described by the equation (1).

$$p = \frac{1}{1 + e^{-kx+b}}. \quad (1)$$

Here, the slope k of the linear part is referred to as *sensitivity*, with higher sensitivity indicating a better ability to distinguish between two directions of motion and better behavioral performance. The intercept b describes the bias of the decision-maker, i.e., the extent to which the decision-maker tends to choose one direction over the other. A good decision-maker should have higher sensitivity and smaller bias.

To ensure consistency in data during model testing, we generated different RDK stimuli using the specialized neuroscience and experimental psychology software PsychoPy [59] with varying parameters and stored the stimuli in the form of three-dimensional arrays.

Computer vision systems that use a camera as the perceptual input typically measure input videos and images in pixels, rather than in degrees as in studies of biological vision. Therefore, the RDK animation used in this study is pixel-based. Specifically,

within a rectangular black background with dimensions of 300 pixels by 300 pixels, a 270-pixel diameter aperture is placed at the center. Inside the aperture, 200 white circles with a diameter of 6 pixels are evenly distributed. Some points (signal dots) are randomly selected to move left or right, while the remaining points (noise dots) are randomly dispersed in all directions. The circles move at a speed of 2 pixels per frame, and their positions are randomly reset every 4 frames or when they move out of the aperture. Following these rules, 120 frames of images are continuously generated and stored in 8-bit grayscale format as a matrix of size $300 \times 300 \times 120$. This animation lasts for 2 seconds on a 60 Hz monitor, matching the stimulus duration of the human behavioral experiment. The RDK dataset contains 100 levels of coherence ranging from 0% to 99% with a step size of 1%. For each coherence level, 10 stimuli were generated for both leftward and rightward motion directions, resulting in a total of 2000 stimuli. This fine-grained variation in coherence levels allows for a detailed analysis of the model’s sensitivity to subtle differences in motion direction.

4.2 The Neural Dynamics Model

The neural dynamics model constructed in this study simulates four key areas of the dorsal pathway involved in motion perception, corresponding to the LGN, V1, MT and LIP regions of the motion perception decision system from primary to high levels (Fig. 1a). We did not directly model lower visual pathway modules (retina, ganglion cells, etc.) in detail, but simplified them into temporal and spatial convolution calculations, directly mapping visual input to the total input current of LGN neurons as the model’s input.

The LGN layer of the model was constructed based on previous research [15, 16]. The LGN is divided into two groups of *ON* and *OFF* neurons adapting the Leaky Integrate-and-Fire (LIF) model, each group containing 10 000 neurons, all with double Gaussian spatial receptive fields (Equation 2, Fig. 1b middle). These neurons cover a

visual angle of 0.35° ($x, y \in [-0.175, 0.175]$ in Equation 2), corresponding to a 9×9 pixel area. They are alternately overlapped and arranged regularly in space (Fig. 1b top), covering the entire 300×300 field of view, forming a two-dimensional plane corresponding to the image space. *ON* and *OFF* neurons have different temporal profiles, with *ON* neurons responding slower than *OFF* neurons (approximately 10 ms, Equation 3, Fig. 1b bottom). Images of 300×300 pixels are convolved spatially with the 9×9 spatial convolution kernels, then the time step is reduced to 2 ms (120 frames expanded to 1000 frames) through nearest-neighbor interpolation, and temporal convolution with a sliding time window of 160 ms is performed. At each time point, two sets of 100×100 convolution results are obtained, which serve as the stimulus-induced current for each neuron in the *ON* and *OFF* neuron groups, respectively, and together with Ornstein–Uhlenbeck noise [60] form the input current of LGN neurons.

$$A(x, y) = \frac{\alpha}{\pi\sigma_\alpha^2} \exp\left(-\frac{x^2 + y^2}{\sigma_\alpha^2}\right) - \frac{\beta}{\pi\sigma_\beta^2} \exp\left(-\frac{x^2 + y^2}{\sigma_\beta^2}\right) \quad (2)$$

where $\alpha = 1$, $\beta = 1$, $\sigma_\alpha = 0.0894$, $\sigma_\beta = 0.1259$ [15].

$$K(t) = \alpha \frac{t^6}{\tau_0^7} \exp\left(-\frac{t}{\tau_0}\right) - \beta \frac{t^6}{\tau_1^7} \exp\left(-\frac{t}{\tau_1}\right) \quad (3)$$

where $\tau_0 = 3.66$, $\tau_1 = 7.16$, $\alpha = 1$, $\beta = 0.8$ for *ON* neurons, and $\alpha = 1$, $\beta = 1$ for *OFF* neurons [15].

The other three brain regions are composed of LIF neuron groups, with each neuron group connected to the neurons in the previous layer with specific structures and probabilities. The V1 area has a total of 5000 neurons, divided into two groups, namely *G1* and *G2*. Each V1 neuron receives input from one *ON* cell and one *OFF* cell arranged in a specific pattern through AMPA synapses. In the LGN projection received by the *G1* group neurons, the *ON* cells are always located to the left of the *OFF*

cells. Similarly, in the LGN projection received by the $G2$ group neurons, the ON cells are always located to the right of the OFF cells (Fig. 1c). The MT area contains two groups of neurons, L and R , each consisting of 400 neurons. The L group neurons receive input from the $G1$ group neurons within a certain receptive field, while the R group neurons receive input from the $G2$ group neurons within the same receptive field. The connections between MT and V1 corresponding neuron groups are also formed by AMPA synapses, with a synaptic conductance of $\bar{g} = 2.0$ nS.

The LIP area is constructed according to the model in literature [21], consisting of excitatory neuron groups A and B (each with 300 neurons) and an inhibitory neuron group I (500 neurons). The A group neurons receive random projections from L , while the B group neurons receive projections from R (50% of neurons for each group) with AMPA synapses. Connections within excitatory groups A , B , as well as connections from excitatory groups to inhibitory neuron group I , are formed by AMPA and NMDA synapses with different temporal characteristics. The inhibitory neuron group I inhibits neurons in groups A and B through GABA synapses. The connection strengths (synaptic conductance coefficients) of the above connections follow a normal distribution $\mathcal{N}(\bar{g}, 0.5\bar{g})$, where the average conductance from MT to LIP is $\bar{g}_{MT} = 0.1$ nS, the average conductance among excitatory neurons in LIP is $\bar{g}_{AMPA} = 0.05$ nS, $\bar{g}_{NMDA} = 0.165$ nS, the average conductance from excitatory neurons to inhibitory neurons in LIP is $\bar{g}_{AMPA} = 0.04$ nS, $\bar{g}_{NMDA} = 0.13$ nS. If the connection strength between two neurons is less than 0, there is no connection (Fig. 1c). Additionally, the connection weights between neurons with the same direction preference increase to $w = 1.3$ times the original weight (*Hebb-strengthened weight*), while the connection weights between neurons with different direction preferences weaken to $w = 0.7$ times the original weight (*Hebb-weakened weight*).

The neurons in the model are all LIF neurons, a commonly used model in computational neuroscience to approximate the behavior of biological neurons. The resting

membrane potential is set to $V_r = -70$ mV, and when the membrane potential of a neuron reaches -50 mV, it fires an action potential, resetting to -55 mV during the refractory period [61]. The LIF model was selected due to its simplicity and computational efficiency, while still capturing essential dynamics of neuronal firing. In addition to synaptic currents and external currents, each neuron receives Ornstein–Uhlenbeck noise, a standard approach for modeling stochastic fluctuations in neuronal input. The time constant of OU noise $\tau = 10$ ms, and mean current of 400 pA with a variance of 100 were chosen to match the noise characteristics observed in biological neurons. For LIP excitatory neurons, a higher mean current of 550 pA was used to simulate the enhanced excitatory drive from other excitatory neurons without direction selectivity. For excitatory neurons, the parameters are $C_m = 0.5$ nF, $g_l = 25$ nS, and refractory period $\tau = 2$ ms. For inhibitory neurons, the parameters are $C_m = 0.2$ nF, $g_l = 20$ nS, and refractory period $\tau = 1$ ms. The AMPA, NMDA, and GABA synapses in the model follow the settings in the literature [21, 62].

We use the overall firing rate of neuron groups A or B in the LIP region as the basis for whether the model makes a decision. When the average firing rate exceeds a threshold (30 Hz) or when the stimulus finishes, the model selects the direction preferred by the neuron group with the higher firing rate as its final output. By simulating the model with each stimulus in the aforementioned RDK dataset, we obtain the accuracy of the model’s decisions and the number of time steps taken for the decision (decision time) under different coherence levels. We can estimate a psychometric function through least squares regression (Equation 1). This method yields behavioral metrics, including the model’s psychometric curve and sensitivity indices.

Furthermore, our model, which possesses a structure akin to biological systems and neurons that mirror those of the biological nervous system, allows for the execution of virtual electrophysiological experiments, recording and analyzing the firing

characteristics of each neuron group in the model, and even performing virtual electrical stimulation on neurons by adding additional current inputs, to study the characteristics of the model (Figs. 2b&c).

Due to the randomness of RDK stimuli and the neural dynamics of the model, to ensure the robustness of the results, each stimulus was repeated twice in the model performance test, and the neural dynamics model was re-initialized and repeated five times. The selection probabilities and average decision times for each coherence level were calculated and estimated using the psychometric curve (Equation 1), and the decision time curve was estimated using a moving median smoothing algorithm with a coherence window of 10% (Fig. 2a upper panel). For human subjects, we conducted a bootstrap analysis on the behavioral data, where the trials of each subject were randomly sampled with replacement, and the median of 1000 bootstrap samples was calculated for each subject. The final average performance over all subjects was plotted.

4.3 A CNN Model for Motion Perception

A convolutional neural network (CNN) model (*MotionNet*) was built similar in structure and scale to the neural dynamics model for comparison (Fig. 4a). The model receives video input with a resolution of 300×300 pixels, processes it through spatial convolutions of 9×9 pixels and temporal convolutions of 10 frames, resulting in two 100×100 feature maps matching the input of LGN neurons. These feature maps are converted to two 50×50 maps using 3×3 convolutional kernels. The two channels are then processed with 11×11 convolutional kernels to generate two 20×20 feature maps. After average pooling along the time dimension, these features are mapped to a 400-dimensional vector by a linear layer, and finally to output neurons using another linear layer. All neurons utilize the *ReLU* activation function except the output layer, which is passed through a softmax transformation for fitting the one-hot encoded direction classification information.

To avoid overfitting the training data and ensure accurate model comparison, *MotionNet* was not directly trained on the RDK dataset. Instead, it utilized generated moving random images as the training data. Specifically, a random grayscale image was generated and stretched randomly. A window covering the image was moved in random directions to obtain the necessary animation data. The speed and direction of movement were randomly assigned, and the training labels (supervision information, moving left or right) were determined by the direction of movement along the horizontal axis.

MotionNet was trained with the cross-entropy loss function and stochastic gradient descent (SGD) method. The initial learning rate was set at 0.01, reduced to 10% at the 5th and 15th epochs. The momentum was set to 0.9, with a batch size of 64, and each epoch contained 500 batches. Training stopped at the 20th epoch. The model from the 20th epoch was selected for testing based on its convergence and stability during training. Similar analyses were then conducted on this model using the RDK dataset, paralleling those applied to the neural dynamics model. This approach ensured a fair comparison between the two models' performance under the same experimental conditions. Specifically, twenty consecutive frames were randomly selected from a 120-frame animation as input for *MotionNet*. The model's choices under various coherences were recorded and psychometric curves were fitted. For result stability, each trial was repeated twice. Unlike the neural dynamics model, *MotionNet*, being a CNN, lacks a concept of time, so we focused on its psychometric curve and related parameters (*sensitivity*).

4.4 RDK Behavioral and Neuroimaging Experiments in Human Subjects

Subjects: Thirty-six subjects participated in this RDK experiment (12 males, 24 females, mean age 29 ± 8 years). Each subject conducted a behavioral experiment with

a series of random-dot motion-direction discrimination tasks (consisting of a learning period, a practice period, and a test period) and an MRI scanning experiment. The MRI experiment consisted of a high-resolution 3D-T1 structural scanning session, a field-map scanning session for image distortion correction, a functional-MRI session for localization of the MT region, two functional-MRI sessions conducting the RDK tasks, and a DWI session for white-matter fiber reconstruction. The study was approved by the Ethics Committee, and informed consent was obtained from each volunteer.

Behavioral experiment: Random-dot stimuli were presented on a monitor at a distance of 57 cm from the subject, with a display resolution of 2560×1440 pixels and a refresh rate of 60 Hz. The stimulus program was written using PsychoPy [59]. The stimuli were a series of circular dots (white dots presented on a black background). Each trial was initialized with a fixation cross ($0.33^\circ \times 0.33^\circ$ dva, lasting for a fixed duration of 500 ms plus a random duration sampled from a uniform distribution with a maximum of 200 ms). Subjects were asked to gaze at the cross. After that, a set of moving dots was presented in a circular area of 5 dva diameter, with a total number of 300 dots and a diameter of 0.04° dva for each of these dots. Some of the dots moved uniformly to the left or right, while the rest of the dots moved randomly with a speed of 3.3° s^{-1} . The positions of all the dots were re-randomized every 5 frames (i.e., the presentation of each dot lasted 5 frames). Subjects were asked to recognize the uniform direction of the moving dots and respond within 2000 ms (Extended Fig. 1a). Each subject first performed a learning period. The proportion of the uniformly moving dots for this period was fixed at a coherence of 80% (i.e., 80% of the dots move in the same direction), and the subject was informed with correct or incorrect feedback after responding to the direction. This period would not terminate until the subject responded correctly 10 consecutive times. After the learning period, the subject entered a practice period. A total of 5 sessions were presented and each session consisted of 70 trials at randomized coherence levels (1%, 2%, 3%, 4%, 5%, 6%, 8%,

10 %, 15 %, 20 %, 25 %, 30 %, 40 % and 50 %, for a total of 14 coherence levels, each of which appeared 5 times). During this period, subjects were also informed of correct or incorrect feedback after responding. Finally, the subject would be presented with a staircase test. The coherence of the trials was set by the staircase method (3-down 1-up method), with an initial coherence of 10 %, a step size of 5 % before the first reversal, and a step size of 1 % after the first reversal. The behavioral experiment was completed after the 20th reversal or 150 trials in total. A psychometric curve was then fitted for each subject's performance, and a coherence corresponding to 79.4% accuracy was estimated as the initial value of coherence in the following MRI experiment.

MRI experiment: MRI experiments were performed using a MAGNETOM Prisma 3T (Siemens Healthcare, Erlangen, Germany) MR scanner with a 64-channel head-neck coil. High-resolution 3D T1 structural images were acquired using the MPRAGE sequence with the following scanning parameters: TR=2530 ms, TE=3.34 ms, TI=1000 ms, flip angle=7°, iPAT=2, FOV=256 × 256 mm², number of slices=192, resolution=1 mm isotropic. Field-map images were scanned using a dual-echo 2D-GRE sequence with the following parameters: TR=747 ms, TE1=4.92 ms, TE2=7.38 ms, FOV=208 × 208 mm², number of slices=72 slices, resolution=2.0 mm isotropic. Functional-MRI was performed using a 2D-GRE-EPI sequence with simultaneous multi-slices scanning with the following parameters: TR=1000 ms, TE=35 ms, flip angle=52°, FOV=208 × 208 mm², number of slices=72 slices, resolution=2.0 mm isotropic, SMS factor=8. The diffusion-weighted images were scanned using a 2D-SE-EPI sequence with simultaneous multi-slices. Scanning parameters: multiple b-values (b=0, 1000, 2500), 96 diffusion directions (32 b=1000 volumes and 64 b=2500 volumes [63]) and 9 b=0 volumes, TR=7400 ms, TE=70 ms, iPAT=2, FOV=204 × 204 mm², number of slices=96 slices, resolution=1.4 mm isotropic, SMS factor=2, partial fourier=6/8, phase-encoding direction=A>>P with only one b=0 volume P<<A.

The MT Localizer task used the classic random-dot expansion-contraction paradigm [64]. The stimuli were presented on a monitor at a distance of 170 cm from the subject, with a resolution of 1920×1080 pixels and a refresh rate of 60 Hz. The program was written using PsychoPy. The stimuli were a series of white circular dots presented on a black background. The experimental paradigm was designed to be an **rArArA** block design, consisting of a 16 s rest block alternating with a 16 s visual stimuli block lasting for a total duration of 112 s. A fixation cross was first presented at the center of the screen for 16 s, and subjects were asked to gaze at the cross; three blocks were then presented. Each block consisted of 200 dots (0.15° dva) presented in a ring ranging from 0.5° dva to 9° dva. A bigger dot of 0.3° dva was presented at the center of the screen, and then all white dots except the central dot started a contraction-expansion movement with a speed of 8° s^{-1} . Subjects were asked to look at the central dot throughout the entire process.

The RDK test task in the MRI scanning used the same paradigm as the behavioral test. Subjects were asked to press two buttons with either the left or right hand. The task adopted an **rABrAB** block design, consisting of a 4 s rest block, a 4 s random viewing block, and a 4 s prompt-and-press block. Each subject went through two sessions, each consisting of 25 trials, and a total duration of 304 s. The experimental stimuli of each trial were consistent with those presented in the behavioral experiment, except that in the prompt-and-press block, a new cue of ‘left-handed’ or ‘right-handed’ appeared at the center of the screen and the subjects followed the cue to press the key with the corresponding hand (Extended Fig. 1b).

In the MRI experiment, we found that the RDK stimulus-induced activation was mainly located in the primary visual cortex, MT, and LIP regions (Extended Fig. 1c, $p < 0.001$, uncorrected, one-sample t -test). This result was consistent with the ROIs modeled in the neural dynamics model of motion perception.

4.5 Neuroimaging Data Analysis Methods

High-resolution 3D-T1 structural images were parcellated into gray matter and white matter and reconstructed into cortex surfaces using Freesurfer [65]. A voxel-level segmentation of brain regions based on the *Destrieux* atlas template [66] was also obtained. Several indices were estimated, including the number of voxels per subregion, cortical area, and average cortical thickness. These processed data and structural features were used in the subsequent correlation analysis.

The fMRI images were corrected using FSL, including slice timing correction, motion correction, and field-map correction. The corrected images were then aligned to the individual space of the T1 structural image. The WM/GM/CSF binary maps were constructed in the structural space for the subsequent GLM analysis to remove white matter and cerebrospinal fluid voxels. In the first-level analysis, the GLM model was used, and the rest, stimuli, and response blocks of each trial were considered as separate regressors. The six motion parameters (three translation and three rotation parameters per frame) and the white matter and cerebrospinal fluid temporal signals were used as nuisance regressors in the model. The GLM model was fitted to each voxel, and the contrast of ‘stimuli – rest’ was constructed to obtain the activation map in z -score. In the second-level analysis, each subject’s activation map in z -score was projected to the individual cortical space (reconstructed cortical surface), and then projected to a standard cortical space (*fsaverage5* template), where the averaged activation map in z -score was obtained by performing a one-sample t -test ($p < 0.001$, uncorrected, Extended Fig. 1c).

The resting-state functional connectivity in this study was obtained from the task-fMRI data [67]. By regressing out the task-dependent signals and filtering the pre-processed results in the 0.01 Hz to 0.08 Hz band, the background signals of the brain were obtained. The resting-state functional connectivity matrix was then calculated using two atlases: the *Destrieux* structural atlas and the *Glasser* functional atlas [68].

Each element of the matrix was used to characterize each ROI pair to correlate with the behavioral results.

Data preprocessing steps for diffusion images included brain extraction, registration to T1 images, field-map top-up correction, and eddy-current correction. We applied a ball-and-stick model to regress the white matter voxels. The model regression of voxels in the white-matter region inferred the white-matter orientation distribution of single voxels, and FA and MD values for each voxel were then obtained [28]. By registering to the white-matter segmentation image, white-matter regions' mean FA and mean MD values (*Destrieux* atlas, threshold: $FA > 0.2$) were calculated for the subsequent correlation analysis. Mean FA and MD values were used to characterize the structural connectivity of white-matter pathways to correlate with the behavioral results.

To visualize the fiber bundles of the subjects, fiber tract reconstruction was performed at the individual level using the quantitative anisotropy of the *DSI Studio*'s gqi inference as a tracking index. Segmented ROIs (lateral occipital and inferior parietal regions) were used as spatial constraints for fiber tracking. Deterministic fiber tracking was performed by the streamline Euler method (tracking threshold =0, angular threshold =0, min length =30 mm, max length =300 mm, seed number =100 000) to obtain the morphology of fiber bundles related to the visual decision-making brain regions in the occipital and parietal lobes of the subjects.

4.6 Neuroimaging-Informed Fine-Tuning

Data analysis: The performance of the subjects in the behavioral RDK experiment was quantitatively analyzed using psychometric curves, and Pearson correlation analysis was performed between the behavioral results and the structural and functional features estimated from the MRI data. For behavioral data, a psychometric curve was

fitted to each subject’s staircase performance, and perceptual ability was determined by taking ‘1 – 79.4% accuracy’.

Pearson correlations were calculated between the above features from structural (number of voxels per subregion, cortical area, average cortical thickness), diffusion (mean FA, mean MD), and functional (resting-state FC elements) images and the perceptual ability indices of the subjects. The ROIs were determined by the parcellation and registration to the *Glasser* atlas and the *Destrieux* atlas in each individual space. We calculated the correlations between the ROIs’ features and the behavioral perceptual abilities ($p < 0.01$ as a threshold of statistical significance).

Connecting physiological data indicators found in magnetic resonance imaging (MRI) with the model is challenging due to the vastly different scales of neural elements involved. In this study, a heuristic approach was used to adjust and assess parameters potentially correlated with structural and functional MRI indicators, inspired by functional analogy. White matter connections found in MRI were simulated by adjusting the mean of the connection parameter distribution for V1 to MT (0.2 to 3.0 with a step size of 0.2), or by adjusting the proportion of connections between MT and LIP (10% to 100% with step 10%). According to *Dale’s principle*, non-positive connection weights were set to zero, equivalent to removing those connections. The adjusted model was retested on the RDK dataset five times, and statistical analysis was performed on the sensitivity of psychometric curves (*slope*) to investigate the impact of parameter adjustments on model performance and identify parameter combinations that improve model performance. Similarly, for functional connections found in fMRI, the synaptic conductance of neurons in MT was altered (0.01 to 0.15 with a step size of 0.01), or the *Hebb-strengthened weight* between LIP excitatory neurons was changed (0.7 to 1.5 with a step size of 0.1) to simulate the neural modulation from other brain regions. The same statistical analysis was conducted to examine the effect of parameter adjustments on model performance.

4.7 Interference Resistance Experiment of the Model

In addition to requiring large amounts of data for training, deep learning models are also prone to biases and are easily affected by noise, resulting in poor transferability, among other issues. To address these problems, we designed a series of perturbation experiments on the neural dynamics model to assess its noise resistance performance.

For each module of the neural dynamics model, we separately tested the effects of deactivating a certain percentage of neurons, discarding a certain percentage of synapses (ranging from 0% to 90% with a step size of 10%), adding a certain level of Gaussian perturbation to the input current of neurons (variance ranging from 0 to 2 times the averaged absolute value of the group’s input current, normal distribution noise with a mean of 0), and adding a certain level of Gaussian perturbation to the connection weights between neurons (variance ranging from 0 to 2 times the averaged absolute value of all connection weights, normal distribution noise with a mean of 0). For each parameter setting, the model’s behavioral performance was evaluated using the RDK dataset. Our analysis concentrated on understanding how changes in model parameters affected sensitivity and overall accuracy. This evaluation highlights the significance of each parameter and demonstrates the resiliency of our model.

For comparison, we conducted similar noise and damage experiments on *MotionNet* as we did on the neural dynamics model. For each layer of *MotionNet*, we separately tested the effects of deactivating a certain percentage of neurons, discarding a certain percentage of connections (ranging from 0% to 90% with a step size of 10%), adding a certain level of Gaussian perturbation to the output of neurons (variance ranging from 0 to 2 times the averaged absolute value of the group’s neuron activation, normal distribution noise with a mean of 0), and adding a certain level of Gaussian perturbation to the connection weights between neurons (variance ranging from 0 to 2 times the averaged absolute value of all connection weights, normal distribution noise with a mean of 0). Due to the fact that the fully connected layer (fc4) of *MotionNet* is

mapped to the output layer with only two neurons, the fc4 connections were neither deactivated nor perturbed during our experiment. After each adjustment of the perturbation parameters, we conducted a complete evaluation on the RDK dataset and calculated the sensitivity of the current model to the parameter changes.

Table 1 *slope of accuracy changes with respect to noise level*

noise type	MotionNet	slope	Neural Dynamics Model	slope
drop connection	conv1	-0.530	LGN-V1	-0.458
drop connection	conv2	-0.574	V1-MT	-0.081
drop connection	fc3	-0.361	MT-LIP	-0.026
add noise to connection	conv1	-0.298	LGN-V1	-0.105
add noise to connection	conv2	-0.263	V1-MT	-0.270
add noise to connection	fc3	-0.041	MT-LIP	-0.006
drop neurons	conv1	-0.594	LGN	-0.456
drop neurons	conv2	-0.411	V1	-0.179
drop neurons	fc3	-0.649	MT	-0.089
drop neurons	fc4	-0.027	LIP	-0.476
add noise to neurons	conv1	-0.004	LGN	-0.304
add noise to neurons	conv2	-0.242	V1	-0.006
add noise to neurons	fc3	-0.122	MT	-0.001
add noise to neurons	fc4	-0.083	LIP	0.004

Extended Data

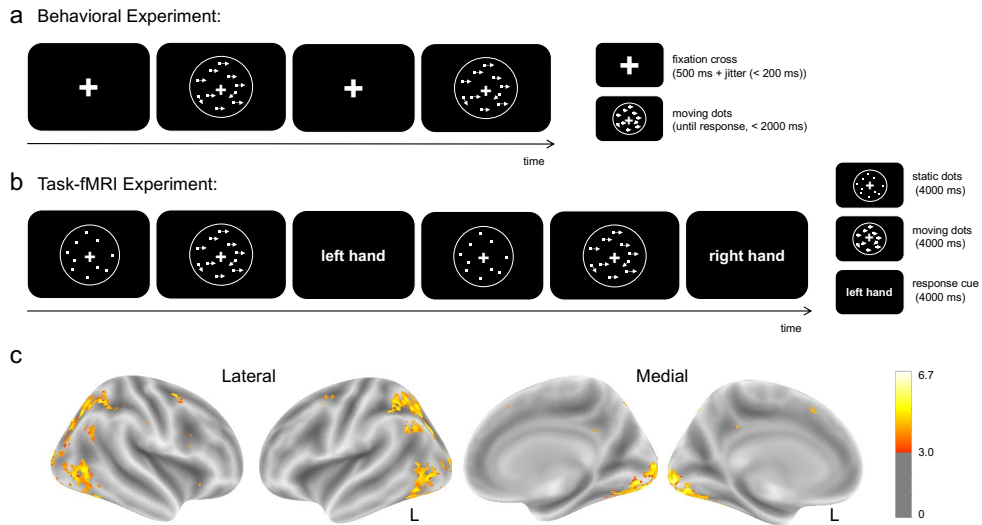


Fig. 1 *Experimental design of the behavioral and MRI tasks.* **a.** The behavioral trial consisted of a fixation cross and a moving-dot stimulus for each trial. Subjects were instructed to fixate on the cross at the center of the screen throughout the entire task and to judge the global motion direction as quickly as possible (within 2000 ms) during the stimulus presentation. **b.** The MRI trial consisted of a fixation cross, a moving-dot stimulus, and a prompt stimulus. Subjects were asked to maintain fixation on the central cross and to press the corresponding button after the left-or-right prompt appeared. **c.** Activation map (z -score) for the task, contrasting 'stimulus' versus 'rest'. Significant activation was observed in the primary visual cortex, MT, and LIP during the task (one-sample t -test, $p < 0.001$, uncorrected).

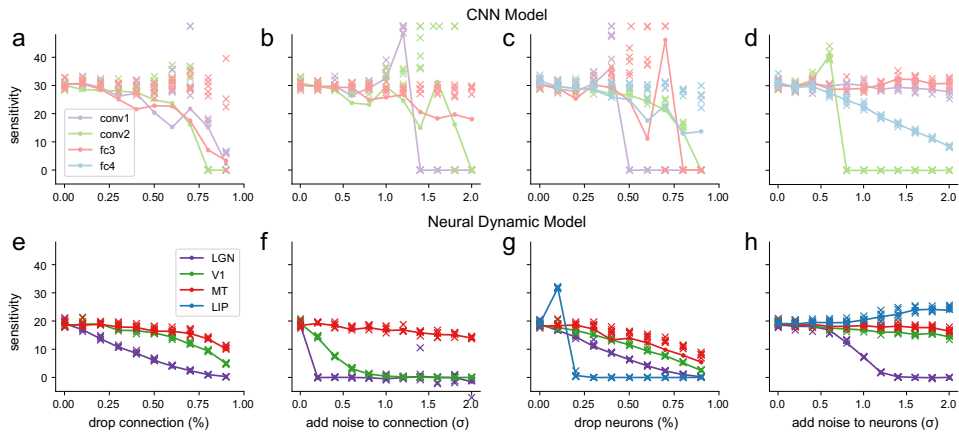


Fig. 2 Sensitivity of CNN and the neural dynamics model changes with perturbation. **a**. Changes in model sensitivity when a certain percentage of connections are dropped in each layer of the CNN; **b**. Changes in model sensitivity when a certain level of Gaussian noise (σ times averaged absolute value) are added to the connection weights of the CNN; **c**. Changes in model sensitivity when a certain percentage of neurons are dropped in each layer of the CNN; **d**. Changes in model sensitivity when a certain level of Gaussian noise (σ times averaged absolute value) are added to the input of neurons of the CNN; **e-h**. The same experiments for the neural dynamics model.

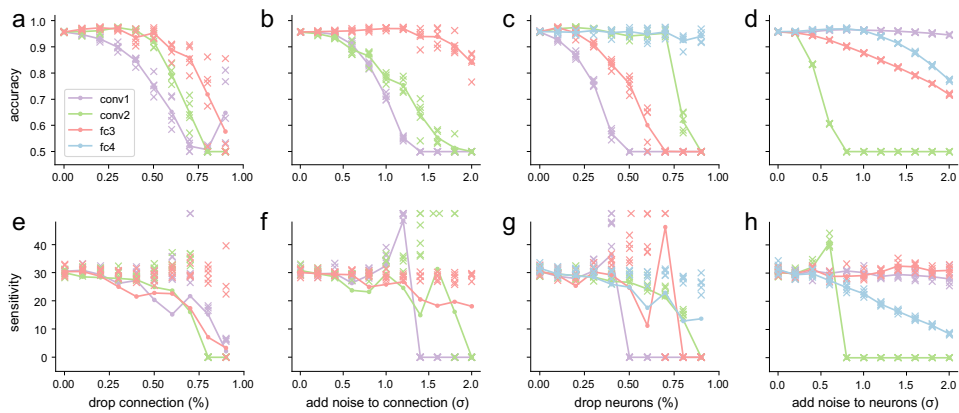


Fig. 3 Perturbation experiment on another CNN model with the same structure. **a-d**. Accuracy of the model changes with noise level; **e-h**. Sensitivity of the model changes with noise level.

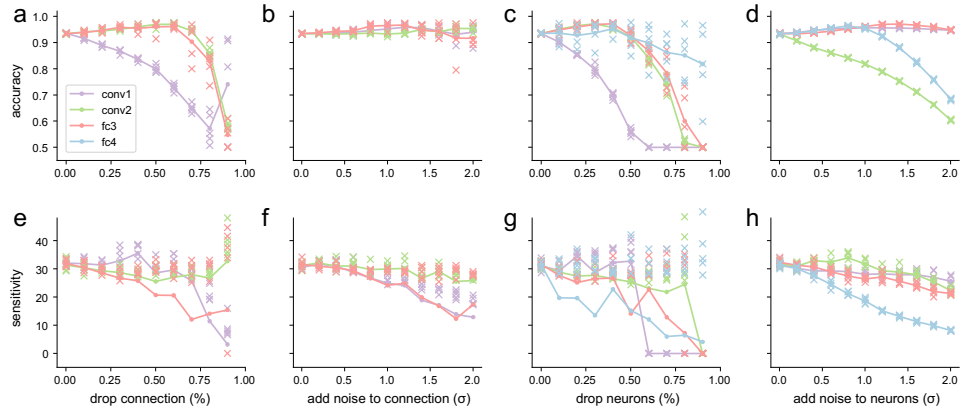


Fig. 4 *Perturbation experiment on another CNN model with the same structure. a-d.* Accuracy of the model changes with noise level; **e-h.** Sensitivity of the model changes with noise level.

Table 1 *Slope of sensitivity changes with respect to noise level*

noise type	MotionNet	slope	Neural Dynamics Model	slope
drop connection	conv1	-17.4	LGN-V1	-22.4
drop connection	conv2	-27.3	V1-MT	-14.3
drop connection	fc3	-7.57	MT-LIP	-8.20
add noise to connection	conv1	-18.1	LGN-V1	-4.65
add noise to connection	conv2	-3.46	V1-MT	-8.39
add noise to connection	fc3	-0.96	MT-LIP	-2.48
drop neurons	conv1	-46.9	LGN	-22.3
drop neurons	conv2	-24.9	V1	-18.2
drop neurons	fc3	-28.3	MT	-11.7
drop neurons	fc4	-4.52	LIP	-24.3
add noise to neurons	conv1	-1.10	LGN	-12.3
add noise to neurons	conv2	-20.5	V1	-2.24
add noise to neurons	fc3	0.87	MT	-0.93
add noise to neurons	fc4	-12.0	LIP	3.02

References

- [1] McCulloch, W. S. & Pitts, W. A logical calculus of the ideas immanent in nervous activity. *The Bulletin of Mathematical Biophysics* **5**, 115–133 (1943).
- [2] Hopfield, J. J. Neural networks and physical systems with emergent collective computational abilities. *Proceedings of the national academy of sciences* **79**, 2554–2558 (1982).
- [3] LeCun, Y., Bottou, L., Bengio, Y. & Haffner, P. Gradient-based learning applied to document recognition. *Proceedings of the IEEE* **86**, 2278–2324 (1998).
- [4] LeCun, Y., Bengio, Y. & Hinton, G. Deep learning. *Nature* **521**, 436–444 (2015).
- [5] Hassabis, D., Kumaran, D., Summerfield, C. & Botvinick, M. Neuroscience-Inspired Artificial Intelligence. *Neuron* **95**, 245–258 (2017).
- [6] Krizhevsky, A., Sutskever, I. & Hinton, G. E. Imagenet classification with deep convolutional neural networks. *Advances in neural information processing systems* **25** (2012).
- [7] Szegedy, C. *et al.* *Going deeper with convolutions.* *2015 IEEE Conference on Computer Vision and Pattern Recognition (CVPR)*, 1–9 (IEEE, Boston, MA, USA, 2015).
- [8] He, K., Zhang, X., Ren, S. & Sun, J. *Deep Residual Learning for Image Recognition.* *2016 IEEE Conference on Computer Vision and Pattern Recognition (CVPR)*, 770–778 (IEEE, Las Vegas, NV, USA, 2016).
- [9] Ji, S., Xu, W., Yang, M. & Yu, K. 3D Convolutional Neural Networks for Human Action Recognition. *IEEE Transactions on Pattern Analysis and Machine Intelligence* **35**, 221–231 (2013).

- [10] Maturana, D. & Scherer, S. *VoxNet: A 3D Convolutional Neural Network for real-time object recognition. 2015 IEEE/RSJ International Conference on Intelligent Robots and Systems (IROS)*, 922–928 (IEEE, Hamburg, Germany, 2015).
- [11] Mishkin, M. & Ungerleider, L. G. Contribution of striate inputs to the visuospatial functions of parieto-occipital cortex in monkeys. *Behavioural Brain Research* **6**, 57–77 (1982).
- [12] Shadlen, M. N. & Newsome, W. T. Neural basis of a perceptual decision in the parietal cortex (area lip) of the rhesus monkey. *Journal of neurophysiology* **86**, 1916–1936 (2001).
- [13] Katz, L. N., Yates, J. L., Pillow, J. W. & Huk, A. C. Dissociated functional significance of decision-related activity in the primate dorsal stream. *Nature* **535**, 285–288 (2016).
- [14] Yates, J. L., Park, I. M., Katz, L. N., Pillow, J. W. & Huk, A. C. Functional dissection of signal and noise in MT and LIP during decision-making. *Nature Neuroscience* **20**, 1285–1292 (2017).
- [15] Chariker, L., Shapley, R., Hawken, M. & Young, L.-S. A theory of direction selectivity for macaque primary visual cortex. *Proceedings of the National Academy of Sciences* **118**, e2105062118 (2021).
- [16] Chariker, L., Shapley, R., Hawken, M. & Young, L.-S. A computational model of direction selectivity in macaque v1 cortex based on dynamic differences between on and off pathways. *Journal of Neuroscience* **42**, 3365–3380 (2022).
- [17] Burr, D. & Thompson, P. Motion psychophysics: 1985–2010. *Vision research* **51**, 1431–1456 (2011).

- [18] Amano, K. *et al.* Human neural responses involved in spatial pooling of locally ambiguous motion signals. *Journal of Neurophysiology* **107**, 3493–3508 (2012).
- [19] Nishida, S., Kawabe, T., Sawayama, M. & Fukiage, T. Motion Perception: From Detection to Interpretation. *Annual Review of Vision Science* **4**, 501–523 (2018).
- [20] Shadlen, M. N. & Newsome, W. T. Motion perception: seeing and deciding. *Proceedings of the National Academy of Sciences* **93**, 628–633 (1996).
- [21] Wang, X.-J. Probabilistic decision making by slow reverberation in cortical circuits. *Neuron* **36**, 955–968 (2002).
- [22] Wong, K.-F. & Wang, X.-J. A recurrent network mechanism of time integration in perceptual decisions. *The Journal of Neuroscience: The Official Journal of the Society for Neuroscience* **26**, 1314–1328 (2006).
- [23] Wang, X.-J. Decision making in recurrent neuronal circuits. *Neuron* **60**, 215–234 (2008).
- [24] Wang, X.-J. Macroscopic gradients of synaptic excitation and inhibition in the neocortex. *Nature Reviews. Neuroscience* **21**, 169–178 (2020).
- [25] Song, H. F., Yang, G. R. & Wang, X.-J. Reward-based training of recurrent neural networks for cognitive and value-based tasks. *eLife* **6**, e21492 (2017).
- [26] Genon, S., Eickhoff, S. B. & Kharabian, S. Linking interindividual variability in brain structure to behaviour. *Nature Reviews Neuroscience* **23**, 307–318 (2022).
- [27] Colom, R., Jung, R. E. & Haier, R. J. General intelligence and memory span: evidence for a common neuroanatomic framework. *Cognitive Neuropsychology* **24**, 867–878 (2007).

- [28] Hämäläinen, S., Sairanen, V., Leminen, A. & Lehtonen, M. Bilingualism modulates the white matter structure of language-related pathways. *NeuroImage* **152**, 249–257 (2017).
- [29] Rice, K. & Redcay, E. Spontaneous mentalizing captures variability in the cortical thickness of social brain regions. *Social Cognitive and Affective Neuroscience* **10**, 327–334 (2015).
- [30] Kanai, R., Bahrami, B., Roylance, R. & Rees, G. Online social network size is reflected in human brain structure. *Proceedings of the Royal Society B: Biological Sciences* **279**, 1327–1334 (2012).
- [31] Forkel, S. J., Friedrich, P., Thiebaut de Schotten, M. & Howells, H. White matter variability, cognition, and disorders: a systematic review. *Brain Structure and Function* 1–16 (2022).
- [32] Schmithorst, V. J. & Yuan, W. White matter development during adolescence as shown by diffusion mri. *Brain and cognition* **72**, 16–25 (2010).
- [33] Kantarci, K. *et al.* White-matter integrity on dti and the pathologic staging of alzheimer’s disease. *Neurobiology of aging* **56**, 172–179 (2017).
- [34] Mechelli, A., Price, C. J., Friston, K. J. & Ashburner, J. Voxel-based morphometry of the human brain: methods and applications. *Current Medical Imaging* **1**, 105–113 (2005).
- [35] Fischl, B. & Dale, A. M. Measuring the thickness of the human cerebral cortex from magnetic resonance images. *Proceedings of the National Academy of Sciences* **97**, 11050–11055 (2000).

- [36] Glasser, M. F. & Van Essen, D. C. Mapping human cortical areas in vivo based on myelin content as revealed by t1-and t2-weighted mri. *Journal of neuroscience* **31**, 11597–11616 (2011).
- [37] Pievani, M. *et al.* Assessment of white matter tract damage in mild cognitive impairment and alzheimer’s disease. *Human brain mapping* **31**, 1862–1875 (2010).
- [38] Sui, J., Huster, R., Yu, Q., Segall, J. M. & Calhoun, V. D. Function–structure associations of the brain: evidence from multimodal connectivity and covariance studies. *Neuroimage* **102**, 11–23 (2014).
- [39] Wang, K. *et al.* Altered functional connectivity in early alzheimer’s disease: A resting-state fmri study. *Human brain mapping* **28**, 967–978 (2007).
- [40] Song, M. *et al.* Brain spontaneous functional connectivity and intelligence. *Neuroimage* **41**, 1168–1176 (2008).
- [41] Hashemi, M. *et al.* The Bayesian Virtual Epileptic Patient: A probabilistic framework designed to infer the spatial map of epileptogenicity in a personalized large-scale brain model of epilepsy spread. *NeuroImage* **217**, 116839 (2020).
- [42] Hanks, T. D., Ditterich, J. & Shadlen, M. N. Microstimulation of macaque area lip affects decision-making in a motion discrimination task. *Nature neuroscience* **9**, 682–689 (2006).
- [43] Briggs, F., Mangun, G. R. & Usrey, W. M. Attention enhances synaptic efficacy and the signal-to-noise ratio in neural circuits. *Nature* **499**, 476–480 (2013).
- [44] Ye, L. & Li, C. Quantifying the Landscape of Decision Making From Spiking Neural Networks. *Frontiers in Computational Neuroscience* **15**, 740601 (2021).

- [45] Lebel, C., Walker, L., Leemans, A., Phillips, L. & Beaulieu, C. Microstructural maturation of the human brain from childhood to adulthood. *NeuroImage* **40**, 1044–1055 (2008).
- [46] Kühn, S., Forlim, C. G., Lender, A., Wirtz, J. & Gallinat, J. Brain functional connectivity differs when viewing pictures from natural and built environments using fMRI resting state analysis. *Scientific Reports* **11**, 4110 (2021).
- [47] Ratcliff, R. A theory of memory retrieval. *Psychological review* **85**, 59 (1978).
- [48] Ratcliff, R. Modeling response signal and response time data. *Cognitive psychology* **53**, 195–237 (2006).
- [49] Ratcliff, R. & McKoon, G. The diffusion decision model: theory and data for two-choice decision tasks. *Neural computation* **20**, 873–922 (2008).
- [50] Usher, M. & McClelland, J. L. The time course of perceptual choice: the leaky, competing accumulator model. *Psychological review* **108**, 550 (2001).
- [51] Tillman, G., Van Zandt, T. & Logan, G. D. Sequential sampling models without random between-trial variability: the racing diffusion model of speeded decision making. *Psychonomic Bulletin & Review* **27**, 911–936 (2020).
- [52] Brown, S. D. & Heathcote, A. The simplest complete model of choice response time: Linear ballistic accumulation. *Cognitive psychology* **57**, 153–178 (2008).
- [53] Wei, H., Bu, Y. & Dai, D. A decision-making model based on a spiking neural circuit and synaptic plasticity. *Cognitive Neurodynamics* **11**, 415–431 (2017).
- [54] Roxin, A. & Ledberg, A. Neurobiological models of two-choice decision making can be reduced to a one-dimensional nonlinear diffusion equation. *PLoS computational biology* **4**, e1000046 (2008).

- [55] Umakantha, A., Purcell, B. A. & Palmeri, T. J. Relating a Spiking Neural Network Model and the Diffusion Model of Decision-Making. *Computational Brain & Behavior* **5**, 279–301 (2022).
- [56] Kim, J.-N. & Shadlen, M. N. Neural correlates of a decision in the dorsolateral prefrontal cortex of the macaque. *Nature neuroscience* **2**, 176–185 (1999).
- [57] Roitman, J. D. & Shadlen, M. N. Response of neurons in the lateral intraparietal area during a combined visual discrimination reaction time task. *Journal of neuroscience* **22**, 9475–9489 (2002).
- [58] Britten, K. H., Shadlen, M. N., Newsome, W. T. & Movshon, J. A. The analysis of visual motion: a comparison of neuronal and psychophysical performance. *Journal of Neuroscience* **12**, 4745–4765 (1992).
- [59] Peirce, J. *et al.* Psychopy2: Experiments in behavior made easy. *Behavior research methods* **51**, 195–203 (2019).
- [60] Lánský, P. & Sacerdote, L. The ornstein–uhlenbeck neuronal model with signal-dependent noise. *Physics Letters A* **285**, 132–140 (2001).
- [61] Troyer, T. W. & Miller, K. D. Physiological gain leads to high isi variability in a simple model of a cortical regular spiking cell. *Neural computation* **9**, 971–983 (1997).
- [62] Jahr, C. E. & Stevens, C. F. Voltage dependence of nmda-activated macroscopic conductances predicted by single-channel kinetics. *Journal of Neuroscience* **10**, 3178–3182 (1990).
- [63] Tian, Q. *et al.* Comprehensive diffusion mri dataset for in vivo human brain microstructure mapping using 300 mt/m gradients. *Scientific Data* **9**, 7 (2022).

- [64] Michels, L., Lappe, M. & Vaina, L. M. Visual areas involved in the perception of human movement from dynamic form analysis. *Neuroreport* **16**, 1037–1041 (2005).
- [65] Fischl, B. Freesurfer. *Neuroimage* **62**, 774–781 (2012).
- [66] Destrieux, C., Fischl, B., Dale, A. & Halgren, E. Automatic parcellation of human cortical gyri and sulci using standard anatomical nomenclature. *Neuroimage* **53**, 1–15 (2010).
- [67] Fox, M. D. *et al.* Combining task-evoked and spontaneous activity to improve pre-operative brain mapping with fmri. *NeuroImage* **124**, 714–723 (2016).
- [68] Glasser, M. F. *et al.* A multi-modal parcellation of human cerebral cortex. *Nature* **536**, 171–178 (2016).